PHYSICAL REVIEW B **108**, 235165 (2023)

Understanding band gaps of lanthanide niobates via first-principles calculations

Haoming Xu,[1,2] Jiajia Cai,[3,*] Weiguo Jing,[4] Xiantao Wei,[1] and Chang-Kui Duan[1,2,5,†]
[1]*CAS Key Laboratory of Microscale Magnetic Resonance, and School of Physical Sciences,*
University of Science and Technology of China, Hefei 230026, China
[2]*CAS Center for Excellence in Quantum Information and Quantum Physics,*
University of Science and Technology of China, Hefei 230026, China
[3]*College of Electrical Engineering, Henan University of Technology, Zhengzhou 450001, China*
[4]*Institute of Condensed Matter and Nanosciences, UCLouvain, Chemin des Étoiles 8, Louvain-la-Neuve 1348, Belgium*
[5]*Hefei National Laboratory, University of Science and Technology of China, Hefei 230088, China*

(Received 10 October 2023; revised 3 December 2023; accepted 6 December 2023; published 21 December 2023)

The optical properties of rare-earth niobates play a crucial role in determining their performance as luminescent materials or host materials. In this study, we performed first-principles calculations based on the hybrid density functional to examine the electronic structures of $LnNbO_4$ (Ln = La–Lu). We found that the usual parameter settings for the functional could not adequately handle the localization and correlation of $4f$ electrons in these full-concentration lanthanide systems, prompting us to adopt a “doping” approach as a more suitable approximation. Our results provide a systematical interpretation of the experimental results on the absorption edge of $LnNbO_4$ (Ln = La–Lu): in addition to the common $O^{2-}-2p$ to $Nb^{5+}-4d$ transition in the $[NbO_4]^{3-}$ group at near 5 eV, the redshifted absorption edge in $EuNbO_4$ is due to $O^{2-}-2p$ to $Eu^{3+}-4f$ charge transfer absorption, while in $CeNbO_4$, $PrNbO_4$, and $TbNbO_4$, the lower energy absorption edges are attributed to the ionization of $Ln^{3+}-4f$ to conduction bands with a mix of $Ln^{3+}-5d$ compositions. This study also provides a general yet simple approximate approach for studying the electronic structures of full-concentrated insulating lanthanide compounds.

DOI: 10.1103/PhysRevB.108.235165

I. INTRODUCTION

Lanthanide-containing luminescent materials have broad applications, including phosphor-converted light-emitting diodes, laser crystals, optical thermometry, biological detection and scanning, and field emission display devices [1–5]. More generally, rare-earth niobates have garnered considerable interest and have been extensively utilized in luminescent materials. Compounds such as $(Y/La/Lu/Gd)NbO_4$, which have full or half-filled outer shells in rare-earth elements, are frequently chosen as hosts for lanthanide dopants. Their wide O→Nb charge transfer (CT) band offers an effective nonradiative method to absorb and subsequently transfer the energy to Ln^{3+} dopants, resulting in efficient luminescence [6–12].

The electronic band gap plays a decisive role in the luminescent properties. Recently, a systematic experimental study on the lanthanide niobates reported the band gaps of 3.25 eV for $CeNbO_4$, 4.35 eV for $LaNbO_4$, 4.55 eV for $YNbO_4$, 4.73 eV for $EuNbO_4$, and 4.90–4.95 eV for $SmNbO_4$, $GdNbO_4$, $DyNbO_4$, $HoNbO_4$, and $YbNbO_4$ [13]. However, there are conflicting reports on the electronic properties of $LnNbO_4$ niobates [14–24]. Moreover, the nature of the electronic transitions that contribute to the absorption edges is not fully understood. In order to interpret the underlying mechanisms of the relevant experimental results, reliable theoretical and computational studies are essential to unravel the decisive factors for the band gaps of the $LnNbO_4$ series.

First-principles calculations based on the supercell method have been effectively used to investigate the electronic properties of semiconductors and insulators, particularly those transitions involving defect levels and host bands [25–34]. Specifically, the projected density of states (PDOS) of each element and orbital has been employed to decipher the composition of bands and to facilitate the interpretation of experimental optical spectra [35–38]. However, the traditional treatment of the orbitals of the elements often gives qualitatively incorrect behaviors when electron localization and related correlation effects are not treated properly.

In this work, the electronic structures of the $LnNbO_4$ niobates are studied via first-principles calculations by taking the locality of $Ln-4f$ orbitals and electron correlation between them into consideration. Based on our calculation results, we analyze the experimental absorption spectra and interpret the transitions contributing to the band gaps [13–24], in conjunction with Dorenbos’ semiempirical chemical shift model [39–41]. Furthermore, the adapted scheme provides a general yet straightforward approximate approach to handle the localization and electron correlation involving $Ln-4f$ orbitals. This approach is anticipated to be useful in the study of full-concentrated insulating lanthanide compounds.

---

[*] jjcai@mail.ustc.edu.cn
[†] ckduan@ustc.edu.cn

II. COMPUTATIONAL DETAILS

The first-principles calculations based on density-functional theory (DFT) are performed using the Vienna *ab initio* simulation package (VASP) [42,43]. Spin-polarized calculations are carried out with the projector augmented wave [44,45] pseudopotentials for atoms, which are obtained from the VASP database as recommended in the manual. The standard pseudopotentials, in which $4f$ orbitals are treated as valence states, are used in calculations involving $4f$ electrons, while the special $4f$-in-core pseudopotentials for trivalent lanthanides (denoted as Ln_3 in VASP), in which the $4f$ electrons are kept frozen in the core, are used in some specific cases for trivalent Ce–Lu ions, which are denoted as $\underline{\text{Ln}}$ by adding an underline in the following text.

The structure and symmetry of compounds play decisive roles in the band structures [46]. Since the monoclinic structure (space group no. 15, $C2/c$) is generally observed for LnNbO_4 and YNbO_4 at room temperature in experiments [47], we adopted the monoclinic structures in our calculations. Each LnNbO_4 primitive cell contains 2 Ln atoms, 2 Nb atoms, and 8 O atoms. To obtain the lattice parameters of the primitive cells, we use the strongly constrained and appropriately normed (SCAN) [48] meta-GGA method with rVV10 nonlocal vdW-DF functional [49] to perform the geometric structure optimizations (atomic positions, cell volume, and cell shape are all allowed to relax). We use an energy cutoff for the plane-wave-basis set of 520 eV and a Γ-centered $4 \times 4 \times 4$ k-point grid. The geometric structures are fully relaxed until the energy change is less than 10^{-6} eV and the maximum Hellmann-Feynman force exerted on each atom is less than 0.01 eV/Å. During the optimizations of lattice parameters, the $4f$-in-core pseudopotentials $\underline{\text{Ln}}$ of trivalent lanthanides are chosen, because the $4f$ states have little effect on the lattice parameters. The optimized lattice parameters are fixed for the subsequent calculations.

In order to obtain the correct band gaps, we perform the hybrid functional calculations using the Heyd-Scuseria-Ernzerhof (HSE) [50] density functional with the fraction of exact exchange $\alpha = 0.25$ and the range-separation parameter $\mu = 0.2$ [51] based on the Perdew-Burke-Ernzerhof revised for solids (PBEsol) [52] exchange-correlation functional, which is referred to as the HSEsol hybrid functional [53]. The HSEsol calculations are performed with a Γ-centered $2 \times 2 \times 2$ k-point grid and an energy cutoff of 400 eV, using the standard pseudopotentials with the $4f$ states treated as valence states for all lanthanides. The HSEsol optimization calculations start from the structure obtained from the SCAN method and only the atomic positions are allowed to relax while the lattice parameters are fixed. Based on the optimized structures, we calculate their band structures and density of states (DOSs) with the HSEsol method.

For calculations involving charged or doping systems, we use a supercell that is expanded from the primitive cell by a transformation ($\mathbf{a}' = -2\mathbf{a} + 2\mathbf{b} - 2\mathbf{c}$, $\mathbf{b}' = -\mathbf{a} - \mathbf{b}$, and $\mathbf{c}' = 2\mathbf{c}$). Such a supercell contains 96 atoms and is approximately cubic in shape, with lattice parameters $\alpha' = \gamma' = 90^\circ$, $\beta' \approx 94^\circ$, and a', b', c' are all around 11 Å. The calculations on supercell are performed using a single Γ k point to sample the Brillouin zone and the other parameters and convergence conditions of all the calculations on supercell are the same as those of the HSEsol calculations on primitive cells.

The charge transition level (CTL) of a defect X between charge states q_1 and q_2 is defined as the Fermi level of the defect systems when the formation energies of defect X in charge states q_1 and q_2 are equal [26]:

$$X^{(q_1/q_2)} = \frac{E_{\text{tot}}[X^{q_1}] - E_{\text{tot}}[X^{q_2}]}{q_2 - q_1}, \tag{1}$$

where $E_{\text{tot}}[X^q]$ is the total energy calculated on a supercell containing the defect X in charge states q, with both image-charge interaction correction (E_{IIC}) and potential alignment correction ($q\Delta V_{\text{NAP}}$) included for charged defects, following the method proposed in Ref. [54], which also applies to anisotropic dielectrics and noncubic cells. The spin-orbit coupling is not considered in our VASP calculation, but introduced by *post hoc* corrections in the same ways as our previous work [55]. For thermodynamic CTL, the $E_{\text{tot}}[X^{q_1}]$ and $E_{\text{tot}}[X^{q_2}]$ are calculated at their respective equilibrium geometric structure, respectively. The relative position between the thermodynamic CTL and valence band maximum (VBM) or conduction band minimum (CBM) can be used to estimate the adiabatic charge transfer (CT) transition energy between X state and CBM or VBM.

In order to calculate the absorption and emission energies of such CT transitions, it is necessary to obtain the optical CTL. We use $X^{q_2}_{@X^{q_1}}$ to represent the electronic ground state of X^{q_2} calculated at the equilibrium geometric structure of (the electronic ground state of) X^{q_1}. The optical CTL of a defect X from charge states q_1 to q_2 (denoted as $X^{(q_1/q_2)}_{\text{opt}}$) is similarly defined, but both the q_1 and q_2 charge states are calculated at the frozen equilibrium geometric structure of the q_1 charge state, i.e., replace $E_{\text{tot}}[X^{q_2}]$ with $E_{\text{tot}}[X^{q_2}_{@X^{q_1}}]$ in Eq. (1). The optical CTLs can be calculated by changing the electron number in the equilibrium structures before or after the transition.

The thermodynamic CTL is independent of the direction of charge change (order of q_1 and q_2), while the optical CTL $X^{(q_1/q_2)}_{\text{opt}}$ is typically higher (when $q_1 > q_2$, adding electrons to X^{q_1}) or lower (when $q_1 < q_2$, removing electrons from X^{q_1}) than the thermodynamic CTL, i.e.,

$$X^{(q_2/q_1)}_{\text{opt}} < X^{(q_2/q_1)} = X^{(q_1/q_2)} < X^{(q_1/q_2)}_{\text{opt}}$$

when $q_1 > q_2$. The differences between $X^{(q_1/q_2)}_{\text{opt}}$ and $X^{(q_2/q_1)}_{\text{opt}}$ caused by the relaxation energies are related to the Stokes shift (the energy difference between optical absorption and emission peaks) of CT transitions [26]. Specifically for Ln^q, the CT absorption involves the transfer of an electron from VBM to Ln^q ($\text{Ln}^q \rightarrow \text{Ln}^{q-1} + h_{\text{VBM}}$) and its photon energy can be estimated via the Frank-Condon principle as $\text{Ln}^{q/(q-1)}_{\text{opt}} - E_{\text{VBM}}$. On the other hand, the CT emission involves the recombination $\text{Ln}^{q-1} + h_{\text{VBM}} \rightarrow \text{Ln}^q$, with an emitted photon energy of approximately $\text{Ln}^{(q-1)/q}_{\text{opt}} - E_{\text{VBM}}$. Similarly, the photon ionization of Ln^q to CBM requires a photon energy of approximately $E_{\text{CBM}} - \text{Ln}^{q/(q+1)}_{\text{opt}}$, while the radiative recombination of an electron at CBM with Ln^{q+1} emits a photon energy of approximately $E_{\text{CBM}} - \text{Ln}^{(q+1)/q}_{\text{opt}}$.

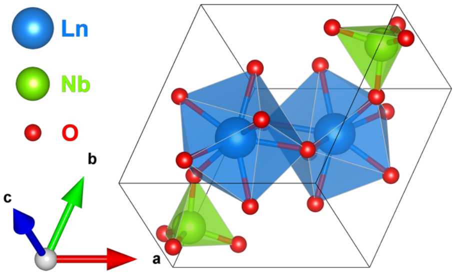

FIG. 1. Primitive cell of $CeNbO_4$ as an example of the geometric structures of the isostructural $LnNbO_4$ series.

III. RESULTS AND DISCUSSION

Figure 1 shows the crystal structure of the $LnNbO_4$ primitive cell (space group no. 15, $C2/c$). The coordination numbers of Ln^{3+} and Nb^{5+} ions are 8 and 4, respectively. The calculated lattice parameters of the primitive cells deviate from the experimental data by about or less than 1% (Supplemental Material Table S1 [56]).

We have calculated the band structures of the $\underline{Ln}NbO_4$ series with the HSEsol method, using $4f$-in-core pseudopotentials for lanthanide ions to simulate the cases where the $Ln-4f$ electrons do not participate in transitions. In these hypothetical cases, the results have similar features to those of $YNbO_4$ (refer to Supplemental Material Figs. S1 and S2 [56] for the details). The valence bands (VBs) are mainly composed of the $2p$ states of O^{2-} with the VBM located at the Γ k point, while the conduction bands (CBs) are mainly composed of the $4d$ states of Nb^{5+} with the CBM located at the Y k point. The band gaps are approximately 5.2–5.3 eV (refer to Supplemental Material Fig. S1 [56]), representing CT transitions from the $O^{2-}-2p$ state to the $Nb^{5+}-4d$ state (hereafter denoted as O→Nb).

To account for the $4f$-related transitions, we have used standard pseudopotentials that incorporate $4f$ valence states. This approach may result in additional bands with $4f$ characters appearing in the forbidden gap that we previously obtained using $4f$-in-core pseudopotentials. We will now proceed with detailed discussions on $EuNbO_4$ and $CeNbO_4$, whose experimental optical band gaps significantly deviate from those of other lanthanide niobates, suggesting potential involvement of $4f$ states in the optical transitions.

A. $EuNbO_4$

The DOSs of $EuNbO_4$ calculated with the HSEsol method are shown in Fig. 2(a). Ignoring the highly localized $4f$ states, the energy gap between the highest $O-2p$ states (VBM) and the lowest $Nb-4d$ states (CBM) is 5.18 eV, consistent with the result obtained from the calculation using the $4f$-in-core pseudopotential. The lowest unoccupied $4f$ states of Eu^{3+} are located in the forbidden gap and the energy gap read off from the difference between the VBM and the lowest unoccupied $Eu-4f$ states is only 2.57 eV (refer to Supplemental Material Fig. S5 [56] for detailed band structures and PDOSs).

To calculate the absorption energy of the CT transition from the $O^{2-}-2p$ state to the $Eu^{3+}-4f$ state (O→Eu), we added one electron to the $EuNbO_4$ supercell to calculate the optical CTL of $Eu^{(3+/2+)}{}_{\mathrm{opt}}$. However, in this calculation, the electron that transferred to the $Eu^{3+}-4f$ state is not localized around a single Eu ion to form a Eu^{2+} with $4f^7$ configuration, but is uniformly distributed among all Eu ions with $4f^{6+\delta}$ configuration (δ is the reciprocal of the number of Eu ions in the supercell). The position of the CTL thus obtained is 2.56 eV (prior to energy correction) relative to the VBM, which aligns closely with the position of the lowest unoccupied $Eu-4f$ states as mentioned earlier, conforming to the characteristic expected of a delocalized electron. This illusion is caused by the inability of the adopted calculation to effectively handle the localization and electron correlation related to highly localized $4f$ electrons. Using larger mixing parameters in the hybrid functional calculations might be able to produce the localized Eu^{2+} $4f^7$ solution, but would lead to significantly overestimated band gaps [66].

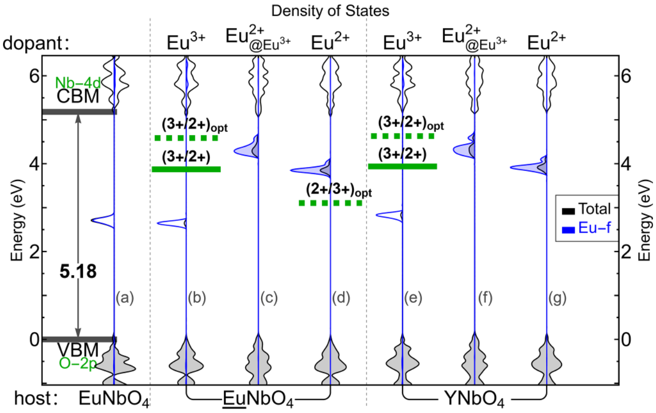

FIG. 2. DOSs of (a) $EuNbO_4$, (b) $\underline{Eu}NbO_4$:Eu^{3+}, (c) $\underline{Eu}NbO_4$:$Eu^{2+}_{@Eu^{3+}}$, (d) $\underline{Eu}NbO_4$:Eu^{2+}, (e) $YNbO_4$:Eu^{3+}, (f) $YNbO_4$:$Eu^{2+}_{@Eu^{3+}}$, and (g) $YNbO_4$:Eu^{2+}. The energies are aligned according to the inner shell $Nb-4s$ orbitals. The PDOSs of the $Eu-4f$ states in (b)–(g) are magnified for clarity. The optical and thermodynamic CTLs of $Eu^{(3+/2+)}$ in $\underline{Eu}NbO_4$ and $YNbO_4$ are also shown for reference.

Here we will present an alternative method to estimate the correct CTL of Eu ions. Since the Eu ions are not in close proximity to each other in $EuNbO_4$, given the highly localized nature of the $4f$ orbitals, the overlap between the $4f$ orbitals of two different Eu ions is negligible and can be disregarded. Consequently, the O→Eu CT transition can be considered as involving only a single Eu ion. The alternative strategy is to use the $4f$-in-core pseudopotential of Eu (denoted as $\underline{Eu}$, or Eu_3 in VASP), in which the $4f$ electrons are kept frozen in the core, for all Eu^{3+} ions in the supercell, with the exception of one Eu^{3+} ion using the standard Eu pseudopotential in which the $4f$ states are treated as valence states. This method, referred to as the "doping" approach in the subsequent discussions, can be perceived as doping a Eu^{3+} ion with $4f$ valence states into the $\underline{Eu}NbO_4$ host supercell devoid of $4f$ valence states (frozen). The addition of one electron to the unoccupied $4f$ orbital of the Eu^{3+} ion at the fixed equilibrium structure results in a Eu^{2+} ion with $4f^7$ configuration, costing an energy termed $Eu^{(3+/2+)}{}_{\mathrm{opt}}$ optical CTL, which is 4.59 eV relative to the VBM. Upon relaxing the positions of atoms in the $\underline{Eu}NbO_4$:Eu^{2+} supercell, we obtain the $\mathrm{Eu}^{(3+/2+)}$ thermodynamic CTL to be 3.87 eV relative to the VBM [Figs. 2(b)–2(d)]. It should be noted that the CTL cannot be directly compared with the generalized Kohn-Sham (gKS) eigenvalues [67,68] in the DOS plot. Only in an exact DFT functional should the (generalized) Kohn-Sham eigenvalues of the highest occupied state be consistent with the ionization energy, i.e., the optical CTL at the given structure. As an illustration, the difference between the highest occupied state of Eu^{2+} and the optical CTL $\mathrm{Eu}^{(2+/3+)}{}_{\mathrm{opt}}$ in Fig. 2(d) can be attributed to the functional adopted being not exact.

Additionally, we also calculate the CTLs of $\mathrm{Eu}^{(3+/2+)}$ in the $\mathrm{YNbO_4{:}Eu^{3+}}$ supercell. The optical CTL of $\mathrm{Eu}^{(3+/2+)}{}_{\mathrm{opt}}$ is obtained to be 4.66 eV relative to the VBM and the thermodynamic CTL of $\mathrm{Eu}^{(3+/2+)}$ to be 3.97 eV relative to the VBM [Figs. 2(e)–2(g)]. The O→Eu CT absorption energy in the $\mathrm{YNbO_4{:}Eu^{3+}}$ thus obtained is consistent with the experimental absorption edges (4.6–4.7 eV [7,69]) of the O→Eu CT transition in the excitation spectrum of $\mathrm{YNbO_4{:}Eu^{3+}}$, validating our calculation results. The experimental excitation spectra of $\mathrm{GdNbO_4{:}Eu^{3+}}$ also exhibit excitation peaks at 4.84 eV [20] and 4.73 eV [12].

Given the similar structures of $\mathrm{YNbO_4}$, $\mathrm{GdNbO_4}$, and $\mathrm{EuNbO_4}$, with only minor differences in lattice parameters and bond lengths, the O→Eu CT transition energies should also be similar among them. These results indicate that the doping approach, which involves freezing the $4f$ electrons of all Eu^{3+} ions except one to circumvent the DFT-related self-interaction errors, is close to the actual situation for obtaining the O→Eu CT energy. We note that this doping approach can be adapted only if the states are highly localized.

Therefore, we attribute the 4.73 eV absorption edge observed in $\mathrm{EuNbO_4}$ absorption spectra [13] to the O→Eu CT transition, whose transition energy is smaller than that of the O→Nb CT transition (approximately 5.18 eV) according to our calculations.

B. $\mathrm{CeNbO_4}$

The DOSs of $\mathrm{CeNbO_4}$ calculated with the HSEsol method are shown in Fig. 3(a). Ignoring the $4f$ states, the energy gap between the VBM and CBM is about 5.37 eV. The highest occupied $4f$ states of Ce^{3+} are located in the forbidden gap and the energy gap between the highest occupied Ce$-4f$ and CBM is about 2.77 eV (refer to Supplemental Material Fig. S4 [56] for detailed band structures and PDOSs).

In a manner akin to the discussion on Eu, we also employed the doping approach to calculate the $\mathrm{Ce}^{(3+/4+)}$ CTL positions in $\underline{\mathrm{Ce}}\mathrm{NbO_4}$. Specifically, we use the $4f$-in-core pseudopotential of Ce (denoted as $\underline{\mathrm{Ce}}$, or Ce_3 in VASP) for all Ce^{3+} ions in the supercell, with the exception of one Ce^{3+} ion using the standard Ce pseudopotential with $4f$ valence states. The positions of the $\mathrm{Ce}^{(3+/4+)}$ optical and thermodynamic CTLs are 4.02 eV and 3.11 eV below the CBM, respectively [Figs. 3(b)–3(d)]. Since the $5d$ orbitals are dispersed in the CBs, it is difficult to directly obtain the $\mathrm{Ce}^{3+}-5d$ excited state. When the $4f$ electron is excited, the $5d$ components will drop to near CBM [refer to Figs. 3(c) and 4]. Therefore, we can approximate the Ce^{3+} $4f\rightarrow5d$ excitation energy by the energy difference between the CBM and the $\mathrm{Ce}^{(3+/4+)}{}_{\mathrm{opt}}$ optical CTL.

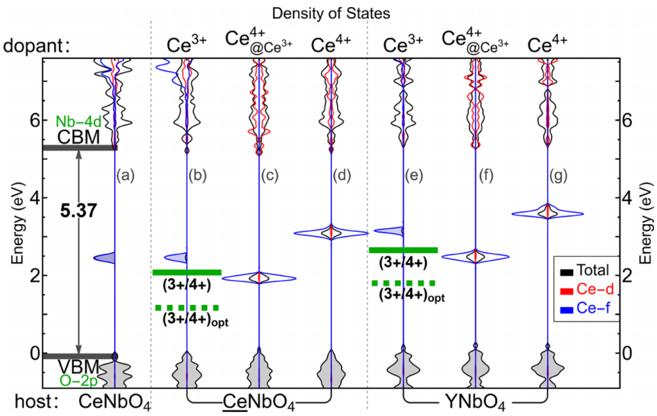

FIG. 3. DOSs of (a) $\mathrm{CeNbO_4}$, (b) $\underline{\mathrm{Ce}}\mathrm{NbO_4{:}Ce^{3+}}$, (c) $\underline{\mathrm{Ce}}\mathrm{NbO_4{:}Ce^{4+}_{@Ce^{3+}}}$, (d) $\underline{\mathrm{Ce}}\mathrm{NbO_4{:}Ce^{4+}}$, (e) $\mathrm{YNbO_4{:}Ce^{3+}}$, (f) $\mathrm{YNbO_4{:}Ce^{4+}_{@Ce^{3+}}}$, and (g) $\mathrm{YNbO_4{:}Ce^{4+}}$. The energies are aligned according to the inner shell Nb$-4s$ orbitals. The PDOSs of the Ce$-4f$ states in (b)–(g) and the Ce$-5d$ states in (a)–(g) are magnified for clarity. The optical and thermodynamic CTLs of $\mathrm{Ce}^{(3+/4+)}$ in $\underline{\mathrm{Ce}}\mathrm{NbO_4}$ and $\mathrm{YNbO_4}$ are also shown for reference.

We have also calculated the CTLs in $\mathrm{YNbO_4{:}Ce^{3+}}$ and obtained the $\mathrm{Ce}^{(3+/4+)}{}_{\mathrm{opt}}$ optical CTL to be 3.57 eV below the CBM and the thermodynamic CTL to be 2.72 eV below the CBM [Figs. 3(e)–3(g)]. The $\mathrm{Ce}^{(3+/4+)}{}_{\mathrm{opt}}$ optical CTL in $\mathrm{YNbO_4{:}Ce^{3+}}$ is 0.45 eV higher than that in $\mathrm{CeNbO_4}$.

The optical absorption band of $\mathrm{CeNbO_4}$ was reported at 3.25 eV [13]. Similarly, the lowest Ce-related absorption band in $\mathrm{YNbO_4{:}Ce^{3+}}$ was reported at a smaller energy of 2.82 eV (440 nm in wavelength) [70]. Based on our calculations on $\mathrm{CeNbO_4}$ and $\mathrm{YNbO_4{:}Ce^{3+}}$, we attribute the absorption in $\mathrm{CeNbO_4}$ to the electric-dipole allowed Ce^{3+} $4f\rightarrow5d$ transition, with $\mathrm{Ce}^{3+}-5d$ dispersed in the conduction band. This is analogous to the assignment in $\mathrm{YNbO_4{:}Ce^{3+}}$, where the Ce$-5d$ orbitals are scattered in the conduction band. Consequently, no emission of Ce^{3+} is observed in $\mathrm{YNbO_4{:}Ce^{3+}}$ [70], since the excited Ce^{3+} ionizes its $5d$ electron to the CB and eventually recombines nonradiatively with the Ce^{4+} leftover to return to the ground state of Ce^{3+}.

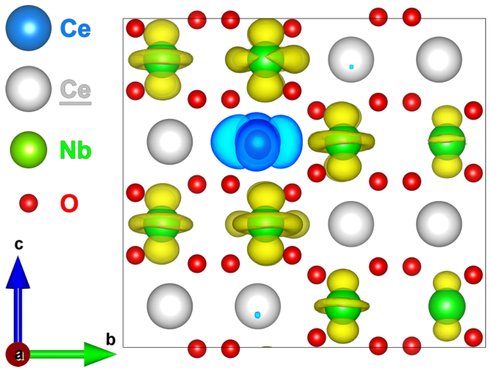

FIG. 4. Square of the absolute value of the wave function of the lowest CB in $\underline{\mathrm{Ce}}\mathrm{NbO_4{:}Ce^{4+}_{@Ce^{3+}}}$. The lowest CB is mainly composed of the $\mathrm{Nb}^{5+}-4d$ states (yellow) and mixed with some $\mathrm{Ce}^{3+}-5d$ (blue) components. The gray-white $\underline{\mathrm{Ce}}$ ions represent the $4f$-in-core Ce^{3+} ions.

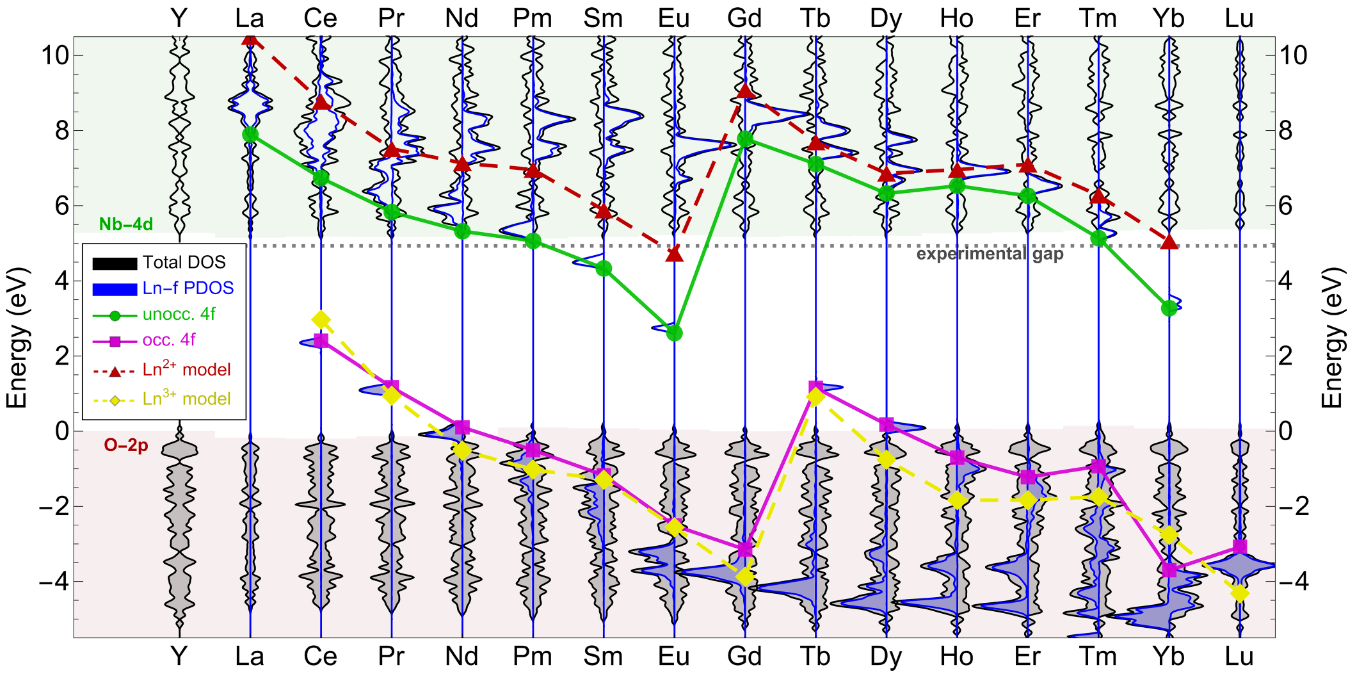

FIG. 5. DOSs of $YNbO_4$ and $LnNbO_4$ for each lanthanide. The lowest unoccupied and the highest occupied $4f$ states of Ln^{3+} in $LnNbO_4$ are represented by solid polylines with circle (green) and square (magenta) markers, respectively. The dashed polylines depict the positions of the Ln^{2+} $4f^n$ levels and the Ln^{3+} $4f^{n-1}$ levels for lanthanides, as per Dorenbos' semiempirical model, marked with triangle (red) and diamond (yellow) markers, respectively. The energies are aligned according to the inner shell Nb$-4s$ orbitals. Ignoring the states made of the $4f$ orbitals of lanthanides, the VBs consist of the O$-2p$ states and the CBs consist of the Nb$-4d$ states. The horizontal gray dotted line indicates the reference experimental optical gap of O→Nb CT transitions in $[NbO_4]^{3-}$ groups, estimated as the average energy of $LnNbO_4$(Ln = Sm, Gd, Dy, Ho, Yb) optical absorption edges.

In addition, the Ce$-4f\rightarrow$CBM transition energies in both $CeNbO_4$ and $YNbO_4$:Ce^{3+}, determined from our CTL calculations, are both about 0.8 eV larger than the energies read off from the experimental optical absorption spectra. We attribute this discrepancy to the employed density functional calculations and inaccuracies in the pseudopotential of Ce.

C. $LnNbO_4$ series

Only those charge transition levels located in the band gap can be directly obtained using Eq. (1). By identifying the optical transitions in $CeNbO_4$ and $EuNbO_4$ and confirming their similarity to isolated activators in $YNbO_4$, we can construct a diagram of the Ln$-4f$ levels using Dorenbos' semiempirical chemical shift model [40,41]. This enables us to evaluate the PDOS results obtained from a conventional calculation for the $LnNbO_4$ series.

Figure 5 depicts the DOSs of $YNbO_4$ and $LnNbO_4$ for each lanthanide calculated with the HSEsol method. The energy reference points for different systems are aligned according to their respective energies of the inner shell Nb$-4s$ orbitals. By either disregarding the localized $4f$ bands or employing the $4f$-in-core pseudopotentials, the fundamental gaps [68] derived approximately from the gap between the gKS eigenvalues of the highest occupied band of $O^{2-}-2p$ nature and the lowest unoccupied band of $Nb^{5+}-4d$ nature are 5.0–5.4 eV. This aligns with the gap of 4.93 eV on average measured by optical absorption spectra in Ref. [13] for $LnNbO_4$ (Ln = Sm, Gd, Dy, Ho, Yb), given that optical gaps are typically smaller than the fundamental gap [68]. Actually, in Dorenbos' semiempirical model applied to $YNbO_4$ [40], the energy of the optical absorption edge is set at 4.9 eV, while the fundamental gap (i.e., the CBM relative to the VBM) is estimated to be 5.3 eV. On the other hand, by using a smaller mixing parameter α of the hybrid density functional, the predicted band gap can be adjusted to a lower value [66]. In this study, we did not aim to fine-tune the α parameter based on band gap values.

Figure 5 also shows the gKS eigenvalues of the highest occupied $4f$ states (magenta solid curve) and the lowest unoccupied $4f$ states (green solid curve) of Ln^{3+} in $LnNbO_4$ obtained from our PDOS calculations. In the full-concentration $LnNbO_4$ system, the trends of these gKS eigenvalues also exhibit a zigzag pattern, similar to the case of lanthanide doping [39].

As references, the positions of the ground state $4f$ levels of Ln^{2+} (red dashed curve) and Ln^{3+} (yellow dashed curve) obtained from Dorenbos' semiempirical model [40] at Ln^{3+} structures are also shown in Fig. 5. The location of the Ln^{3+} curve is established similarly to that of $YNbO_4$ [40] and the location of the Ln^{2+} curve with respect to VBM is established from the CT O→Eu CT absorption energy [13]. The gKS eigenvalues of the highest occupied and the lowest unoccupied $4f$ states obtained from the DOS plot are similar in trends to the $4f$ levels obtained from the semiempirical model, differing by an overall shift. It should be noted that

Dorenbos' semiempirical model describes the trends of lanthanides doped in the same hosts, while the hosts corresponding to the full-concentration cases have slight differences in lattice parameters and bond lengths.

Relative to the semiempirical curve, the gKS eigenvalues of the unoccupied $4f$ states of lanthanides with less-than-half-filled $4f$ shells (La–Eu) are on average about 1.9 eV lower, while those in the right half (Gd–Yb) are about 0.5 eV to 1.5 eV lower. The gKS eigenvalues of the occupied $4f$ orbitals are close to those of the semiempirical curve for Ce–Tb, but about 1.0 eV higher for Dy–Tm and Lu, with the exception of Yb, which is lower than that of the semiempirical curve. The overall relative overestimation of those lanthanides with more-than-half-filled $4f$ shells has also been observed in our previous work on SrB_4O_7 doped with lanthanides [55].

It should be noted that the comparison between the gKS eigenvalues of $4f$ states obtained from the PDOS plot and the $4f$ levels obtained from the semiempirical model is only intended to demonstrate the similarity in their trends. The numerical differences between them depend on the functional used and have no physical significance. A much larger mixing parameter α would be required for $LnNbO_4$ systems to produce the frontier $4f$ orbitals closer to fulfilling the generalized Koopmans' theorem [71] under the scheme of gKS formalism. However, the current HSEsol hybrid density functional parameters have produced sufficiently reasonable estimation of the O$-2p$ to Nb$-4d$ CT transition energies along the lanthanide niobates, while a much larger α would significantly overestimate these energies, incompatible with experimental observations.

Combining our calculations and experiments, we attribute the absorption edge of $EuNbO_4$ to the CT transition from O^{2-} to Eu^{3+}. This is substantiated by the lower absorption edge of $EuNbO_4$ compared to those of most other $LnNbO_4$ in the experimental absorption spectra [13]. Furthermore, it is consistent with our calculations that O→Eu CT absorption energy is smaller than the O→Nb energy gap. Additionally, the positions of the Yb$-4f$ states are anomalously lower in our calculations. This can be attributed to the deficiencies in the troublesome pseudopotential of Yb with an almost full $4f$ shell. We have calculated the O→Yb CT absorption energy via the optical CTL in the $\underline{\mathrm{Yb}}NbO_4$ supercell and obtained the value of 5.31 eV, which is slightly higher than the O→Nb CT absorption energy. Therefore, we attribute the absorption edge of $YbNbO_4$ to the O→Nb CT absorption, with the possible overlapped contribution of the O→Yb CT absorption. The experimentally measured band gap of $YbNbO_4$ is similar to those of other $LnNbO_4$ [13], which supports our assignment.

The absorption edge of $CeNbO_4$ is attributed to the transition from $Ce^{3+}-4f$ to CB via $4f \rightarrow 5d$ transition and the transition energy can be approximated by the energy difference between the lowest Ce$-4f$ states and the CBM (Nb$-4d$ mixed with Ce$-5d$). Moreover, the experiments conducted on $YNbO_4$:Pr^{3+} reported the Pr^{3+} $4f^2 \rightarrow 4f^1 5d^1$ excitation at 4.20 eV (295 nm [70]) and the Pr^{3+} intervalence charge transfer (IVCT) band at 4.17 eV (33600 cm^{-1} [72]), while the experiments conducted on $YNbO_4$:Tb^{3+} reported the Tb^{3+} $4f^8 \rightarrow 4f^7 5d^1$ excitation at 4.13 eV (300 nm [73]) and the Tb^{3+} IVCT band at 4.00 eV (310 nm [74]). Similarly, combining these experiments and Fig. 5, the absorption edges of $PrNbO_4$ and $TbNbO_4$ are also attributed to the transitions from $Ln^{3+}-4f$ to CB (both $4f \rightarrow 5d$ transition and IVCT are possible), which are smaller than O→Nb CT absorption energy.

For the remaining lanthanide elements (Ln = La, Nd, Pm, Sm, Gd, Dy, Ho, Er, Tm, Yb, Lu), the energies of the O→Ln CT absorption are predicted to be higher than those of the O→Nb CT absorption, as shown by the red triangle markers being above the Nb$-4d$ CBM in Fig. 5. Therefore, we attribute the reported absorption edges of these $LnNbO_4$ (except for Ln = Pm being radioactive without experimental result) to the CT transitions from O^{2-} ligands to central Nb^{5+} atoms in the $[NbO_4]^{3-}$ groups. This is also consistent with the experimentally reported band gaps of $SmNbO_4$, $GdNbO_4$, $DyNbO_4$, $HoNbO_4$, and $YbNbO_4$, which are all in the range of 4.90–4.95 eV [13].

Additionally, the experimentally reported band gaps are 4.35 eV for $LaNbO_4$ and 4.55 eV for $YNbO_4$ [13], which are smaller than the energy range of the O→Nb CT transition in the $[NbO_4]^{3-}$ groups. However, according to our PDOS calculations in the pure $LaNbO_4$ and $YNbO_4$ crystal (Supplemental Material Figs. S2 and S3 [56]), the $4f$ or $5d$ orbitals of La^{3+} and the $4d$ orbitals of Y^{3+} are well above the CBM of Nd$-4d$ nature. Considering the possible influence of defects on experimental samples and combining with other experimental reports [16], we attribute the reported smaller band gap of $LaNbO_4$ to the presence of distorted NbO_6^{7-} octahedrons (with absorbing edges at 300 nm [16]) in the $LaNbO_4$ sample synthesized at 1200 °C. With regard to $YNbO_4$, various unidentified defects, such as vacancies and antisites, can produce defect states in the band gap.

IV. CONCLUSIONS

In this work, we have systematically studied the electronic structures of lanthanide niobates via the HSEsol version of the hybrid density functional. Based on our calculation results, we analyzed the experimental absorption spectra and provided a consistent interpretation of the measured absorption edges. For $LnNbO_4$ (Ln = La, Nd, Sm, Gd, Dy, Ho, Er, Tm, Yb, Lu), the absorption edges are attributed to the CT transition of the $[NbO_4]^{3-}$ group, where an electron is transferred from $O^{2-}-2p$ to $Nb^{5+}-4d$. However, the absorption edge of $EuNbO_4$ is attributed to the CT transition from $O^{2-}-2p$ to $Eu^{3+}-4f$, while the absorption edges of $CeNbO_4$, $PrNbO_4$, and $TbNbO_4$ are attributed to the transitions from $Ln^{3+}-4f$ to CB, which contains the compositions of $Ln^{3+}-5d$ orbitals. In addition, the absorption in $PmNbO_4$ is predicted to be the CT of $[NbO_4]^{3-}$.

We noted that, due to strong electron correlation and localization of $4f$ orbitals, adding or removing a $4f$ electron should be considered as happening to a single Ln ion at a time, rather than fractionally to many Ln ions. Hence a more appropriate choice is to use the $4f$-in-core pseudopotentials for all lanthanide ions in the supercell except one lanthanide with standard pseudopotential. This mimics the change in number of localized $4f$ electrons only for the designated Ln ion.

ACKNOWLEDGMENTS

This work was supported by the National Natural Science Foundation of China (Grants No. 12304445, No. 62375255, and No. 11974338), Innovation Program for Quantum Science and Technology (Grants No. 2021ZD0302200 and No. 2021ZD0303204), and the National Key Research and Development Program of China (Grant No. 2018YFA0306600). The numerical calculations were performed on the supercomputing system in the Supercomputing Center of the University of Science and Technology of China. We used VASPKIT [75] and VESTA [76] to display our results.

---

[1] G. Li, Y. Tian, Y. Zhao, and J. Lin, Recent progress in luminescence tuning of Ce^{3+} and Eu^{2+}-activated phosphors for pc-WLEDs, Chem. Soc. Rev. **44**, 8688 (2015).

[2] H. Suo, X. Zhao, Z. Zhang, Y. Wang, J. Sun, M. Jin, and C. Guo, Rational design of ratiometric luminescence thermometry based on thermally coupled levels for bioapplications, Laser Photon. Rev. **15**, 2000319 (2021).

[3] N. da Silva Marques, E. J. Nassar, M. Verelst, R. Mauricot, H. Brunckova, and L. A. Rocha, Effect of ytterbium amount on $LaNbO_4$:Tm^{3+}, Yb^{3+} nanoparticles for bio-labelling applications, Adv. Med. Sci. **65**, 324 (2020).

[4] P. Pei, Y. Chen, C. Sun, Y. Fan, Y. Yang, X. Liu, L. Lu, M. Zhao, H. Zhang, D. Zhao, X. Liu, and F. Zhang, X-ray-activated persistent luminescence nanomaterials for NIR-II imaging, Nat. Nanotechnol. **16**, 1011 (2021).

[5] Z. Wang, Q. Meng, C. Wang, D. Fan, and Y. Wang, Full color-emitting (Y,Tb,Eu)NbO_4 nanophosphors: calcination-assisted hydrothermal synthesis, energy interaction, and application in deep UV chip-based WLEDs, J. Mater. Chem. C **8**, 14548 (2020).

[6] G. Blasse and A. Bril, Luminescence phenomena in compounds with fergusonite structure, J. Lumin. **3**, 109 (1970).

[7] Y. Li, J. Xiao, Y. Zhou, D. Meng, A. Che, and L. Zhao, $YNbO_4$:RE^{3+} (RE = Eu, Sm, Pr, Dy) phosphors: The luminescence properties and The energy transfer between the host and the RE^{3+} ions, Optik **208**, 164126 (2020).

[8] Y. Luo, D. Zhang, S. Xu, L. Li, L. Chen, and H. Guo, Optical thermometry based on Bi^{3+}, Ln^{3+} co-doped $YNbO_4$ (Ln = Dy, Eu) phosphors, J. Lumin. **257**, 119780 (2023).

[9] X. Liu, Y. Lü, C. Chen, S. Luo, Y. Zeng, X. Zhang, M. Shang, C. Li, and J. Lin, Synthesis and luminescence properties of $YNbO_4$:A (A = Eu^{3+} and/or Tb^{3+}) nanocrystalline phosphors via a sol-gel process, J. Phys. Chem. C **118**, 27516 (2014).

[10] Y. Lü, X. Tang, L. Yan, K. Li, X. Liu, M. Shang, C. Li, and J. Lin, Synthesis and luminescent properties of $GdNbO_4$:RE^{3+} (RE = Tm, Dy) nanocrystalline phosphors via the sol-gel process, J. Phys. Chem. C **117**, 21972 (2013).

[11] T. Wang, Y. Hu, L. Chen, X. Wang, and M. He, A white-light emitting phosphor $LuNbO_4$:Dy^{3+} with tunable emission color manipulated by energy transfer from NbO_4^{3-} groups to Dy^{3+}, J. Lumin. **181**, 189 (2017).

[12] X. Liu, C. Chen, S. Li, Y. Dai, H. Guo, X. Tang, Y. Xie, and L. Yan, Host-sensitized and tunable luminescence of $GdNbO_4$:Ln^{3+} (Ln^{3+} = Eu^{3+}/Tb^{3+}/Tm^{3+}) nanocrystalline phosphors with abundant color, Inorg. Chem. **55**, 10383 (2016).

[13] A. B. Garg, D. Vie, P. Rodriguez-Hernandez, A. Muñoz, A. Segura, and D. Errandonea, Accurate determination of the bandgap energy of the rare-earth niobate series, J. Phys. Chem. Lett. **14**, 1762 (2023).

[14] M. Arai, Y. X. Wang, S. Kohiki, M. Matsuo, H. Shimooka, T. Shishido, and M. Oku, Dielectric property and electronic structure of $LaNbO_4$, Jpn. J. Appl. Phys. **44**, 6596 (2005).

[15] S. Ding, H. Zhang, Y. Chen, Q. Zhang, R. Dou, W. Liu, G. Sun, and D. Sun, Structure, electronic and optical properties of $LaNbO_4$: An experimental and first-principles study, Solid State Commun. **277**, 7 (2018).

[16] Y. Hsiao, T. Fang, Y. Chang, Y. Chang, C. Liu, L. Ji, and W. Jywe, Structure and luminescent properties of $LaNbO_4$ synthesized by sol-gel process, J. Lumin. **126**, 866 (2007).

[17] C. Nico, M. R. N. Soares, F. M. Costa, T. Monteiro, and M. P. F. Graça, Structural, optical, and electrical properties of $SmNbO_4$, J. Appl. Phys. **120**, 051708 (2016).

[18] J. C. Peixoto, A. Dias, F. M. Matinaga, and K. P. Siqueira, Luminescence properties of $PrNbO_4$ and $EuNbO_4$ orthoniobates and investigation of their structural phase transition by high-temperature Raman spectroscopy, J. Lumin. **238**, 118284 (2021).

[19] M. Hirano and K. Ishikawa, Direct synthesis of nanocrystalline $GdNbO_4$ and $GdNbO_4$-based phosphors doped with Eu^{3+} through hydrothermal route, J. Ceram. Soc. Jpn. **124**, 42 (2016).

[20] X. Xiao and B. Yan, Synthesis and luminescent properties of novel $RENbO_4$:Ln^{3+} (RE=Y,Gd,Lu; Ln=Eu,Tb) microcrystalline phosphors, J. Non-Cryst. Solids **351**, 3634 (2005).

[21] M. Hirano and H. Dozono, Hydrothermal formation and characteristics of rare-earth niobate phosphors and solid solutions between $YNbO_4$ and $TbNbO_4$, Mater. Chem. Phys. **143**, 860 (2014).

[22] J. Guo, J. Ren, R. Cheng, Q. Dong, C. Gao, X. Zhang, and S. Guo, Growth, structural and thermophysical properties of $TbNbO_4$ crystals, CrystEngComm **20**, 1455 (2018).

[23] Z. Zhang, L. Guo, H. Sun, D. Peng, H. Zou, N. Sun, Q. Zhang, and X. Hao, Rare earth orthoniobate photochromics with self-activated upconversion emissions for high-performance optical storage applications, J. Mater. Chem. C **9**, 13841 (2021).

[24] M. Baran, K. Belikov, A. Kissabekova, A. Krasnikov, A. Lushchik, E. Mihokova, V. Tsiumra, L. Vasylechko, S. Zazubovich, and Y. Zhydachevskyy, Origin of luminescence in Bi^{3+}-doped lanthanide niobates, J. Alloy. Compd. **859**, 157800 (2021).

[25] M. Rohlfing and S. G. Louie, Electron-hole excitations and optical spectra from first principles, Phys. Rev. B **62**, 4927 (2000).

[26] C. Freysoldt, B. Grabowski, T. Hickel, J. Neugebauer, G. Kresse, A. Janotti, and C. G. Van de Walle, First-principles calculations for point defects in solids, Rev. Mod. Phys. **86**, 253 (2014).

[27] N. Mardirossian and M. Head-Gordon, Thirty years of density functional theory in computational chemistry: an overview and

extensive assessment of 200 density functionals, Mol. Phys. **115**, 2315 (2017).

[28] Y. Yang, J. Liu, B. Zhang, and F. Liu, Mechanistic studies of mercury adsorption and oxidation by oxygen over spinel-type $MnFe_2O_4$, J. Hazard. Mater. **321**, 154 (2017).

[29] Z. Feng, B. Lou, Q. Chen, M. Yin, C.-G. Ma, and C.-K. Duan, Self-activated and bismuth-related photoluminescence in rare-earth vanadate, niobate, and tantalate series–A first-principles study, Inorg. Chem. **60**, 16614 (2021).

[30] J. Cai and Y. Y. Yeung, Tuning scintillation properties of Lu_2SiO_5 by Ce and Ca codoping, Phys. Rev. B **107**, 085149 (2023).

[31] J. Kapeghian and A. S. Botana, Electronic structure and magnetism in infinite-layer nickelates RNiO$_2$ (R = La–Lu), Phys. Rev. B **102**, 205130 (2020).

[32] K. Hoang, Rare-earth defects in GaN: A systematic investigation of the lanthanide series, Phys. Rev. Mater. **6**, 044601 (2022).

[33] R. Gillen, S. J. Clark, and J. Robertson, Nature of the electronic band gap in lanthanide oxides, Phys. Rev. B **87**, 125116 (2013).

[34] P. Saghy, A. M. Brown, C. Chu, L. C. Dube, W. Zheng, J. R. Robinson, and O. Chen, Lanthanide double perovskite nanocrystals with emissions covering the UV-C to NIR spectral range, Adv. Opt. Mater. **11**, 2300277 (2023).

[35] Y. Imai and A. Watanabe, Comparison of electronic structures of doped ZnO by various impurity elements calculated by a first-principle pseudopotential method, J. Mater. Sci.: Mater. Electron. **15**, 743 (2004).

[36] J.-M. Zhang, F.-L. Zheng, Y. Zhang, and V. Ji, First-principles study on electronic properties of SiC nanoribbon, J. Mater. Sci. **45**, 3259 (2010).

[37] A. Khireddine, A. Bouhemadou, S. Alnujaim, N. Guechi, S. Bin-Omran, Y. Al-Douri, R. Khenata, S. Maabed, and A. Kushwaha, First-principles predictions of the structural, electronic, optical and elastic properties of the zintl-phases AE_3GaAs_3 (AE = Sr, Ba), Solid State Sci. **114**, 106563 (2021).

[38] S. Ding, H. Zhang, W. Liu, D. Sun, and Q. Zhang, Experimental and first principle investigation the electronic and optical properties of $YNbO_4$ and $LuNbO_4$ phosphors, J. Mater. Sci.: Mater. Electron **29**, 11878 (2018).

[39] P. Dorenbos, Modeling the chemical shift of lanthanide $4f$ electron binding energies, Phys. Rev. B **85**, 165107 (2012).

[40] P. Dorenbos, A. Krumpel, E. van der Kolk, P. Boutinaud, M. Bettinelli, and E. Cavalli, Lanthanide level location in transition metal complex compounds, Opt. Mater. **32**, 1681 (2010).

[41] P. Dorenbos, Improved parameters for the lanthanide $4f^q$ and $4f^{q-1}5d$ curves in HRBE and VRBE schemes that takes the nephelauxetic effect into account, J. Lumin. **222**, 117164 (2020).

[42] G. Kresse and J. Hafner, *Ab initio* molecular dynamics for liquid metals, Phys. Rev. B **47**, 558 (1993).

[43] G. Kresse and J. Hafner, *Ab initio* molecular-dynamics simulation of the liquid-metal–amorphous-semiconductor transition in germanium, Phys. Rev. B **49**, 14251 (1994).

[44] P. E. Blöchl, Projector augmented-wave method, Phys. Rev. B **50**, 17953 (1994).

[45] G. Kresse and D. Joubert, From ultrasoft pseudopotentials to the projector augmented-wave method, Phys. Rev. B **59**, 1758 (1999).

[46] E. O. Filatova and A. S. Konashuk, Interpretation of the changing the band gap of Al_2O_3 depending on its crystalline form: Connection with different local symmetries, J. Phys. Chem. C **119**, 20755 (2015).

[47] S. W. Arulnesan, P. Kayser, J. A. Kimpton, and B. J. Kennedy, Studies of the fergusonite to scheelite phase transition in $LnNbO_4$ orthoniobates, J. Solid State Chem. **277**, 229 (2019).

[48] J. Sun, A. Ruzsinszky, and J. P. Perdew, Strongly constrained and appropriately normed semilocal density functional, Phys. Rev. Lett. **115**, 036402 (2015).

[49] H. Peng, Z.-H. Yang, J. P. Perdew, and J. Sun, Versatile van der waals density functional based on a meta-generalized gradient approximation, Phys. Rev. X **6**, 041005 (2016).

[50] J. Heyd, G. E. Scuseria, and M. Ernzerhof, Hybrid functionals based on a screened Coulomb potential, J. Chem. Phys. **118**, 8207 (2003).

[51] A. V. Krukau, O. A. Vydrov, A. F. Izmaylov, and G. E. Scuseria, Influence of the exchange screening parameter on the performance of screened hybrid functionals, J. Chem. Phys. **125**, 224106 (2006).

[52] J. P. Perdew, A. Ruzsinszky, G. I. Csonka, O. A. Vydrov, G. E. Scuseria, L. A. Constantin, X. Zhou, and K. Burke, Restoring the density-gradient expansion for exchange in solids and surfaces, Phys. Rev. Lett. **100**, 136406 (2008).

[53] L. Schimka, J. Harl, and G. Kresse, Improved hybrid functional for solids: The HSEsol functional, J. Chem. Phys. **134**, 024116 (2011).

[54] T. R. Durrant, S. T. Murphy, M. B. Watkins, and A. L. Shluger, Relation between image charge and potential alignment corrections for charged defects in periodic boundary conditions, J. Chem. Phys. **149**, 024103 (2018).

[55] H. Xu, W. Jing, M. Liu, M. Yin, and C.-K. Duan, First-principles rationalization of self-reduction and lanthanide defect levels in SrB_4O_7, Phys. Rev. B **107**, 075145 (2023).

[56] See Supplemental Material at http://link.aps.org/supplemental/10.1103/PhysRevB.108.235165 for detailed information on the lattice parameters' optimizations, positions of lanthanides' $4f$ states, band structures, and density of states for $LnNbO_4$ and $YbNbO_4$, which contains Refs. [57–65].

[57] P. Sarin, R. W. Hughes, D. R. Lowry, Z. D. Apostolov, and W. M. Kriven, High-temperature properties and ferroelastic phase transitions in rare-earth niobates ($LnNbO_4$), J. Am. Ceram. Soc. **97**, 3307 (2014).

[58] S. Tsunekawa, T. Kamiyama, K. Sasaki, H. Asano, and T. Fukuda, Precise structure analysis by neutron diffraction for $RNbO_4$ and distortion of NbO_4 tetrahedra, Acta Crystallogr. Sect. A **49**, 595 (1993).

[59] A. Santoro, M. Marezio, R. Roth, and D. Minor, Neutron powder diffraction study of the structures of $CeTaO_4$, $CeNbO_4$, and $NdTaO_4$, J. Solid State Chem. **35**, 167 (1980).

[60] C. Keller, Über ternäre Oxide des Niobs und Tantals vom Typ ABO_4, Z. Anorg. Allg. Chem. **318**, 89 (1962).

[61] B. G. Mullens, M. Avdeev, H. E. A. Brand, S. Mondal, G. Vaitheeswaran, and B. J. Kennedy, Insights into the structural variations in $SmNb_{1-x}Ta_xO_4$ and $HoNb_{1-x}Ta_xO_4$ combined experimental and computational studies, Dalton Trans. **50**, 9103 (2021).

[62] A. B. Garg, R. Rao, D. Errandonea, J. Pellicer-Porres, D. Martinez-Garcia, and C. Popescu, Pressure-induced instability of the fergusonite phase of $EuNbO_4$ studied by *in situ* Raman

spectroscopy, x-ray diffraction, and photoluminescence spectroscopy, J. Appl. Phys. **127**, 175905 (2020).

[63] M. P. F. Graça, M. V. Peixoto, N. Ferreira, J. Rodrigues, C. Nico, F. M. Costa, and T. Monteiro, Optical and dielectric behaviour of $EuNbO_4$ crystals, J. Mater. Chem. C **1**, 2913 (2013).

[64] A. Dwivedi, K. Mishra, and S. B. Rai, Multi-modal luminescence properties of RE^{3+} (Tm^{3+}, Yb^{3+}) and Bi^{3+} activated $GdNbO_4$ phosphors-upconversion, downshifting and quantum cutting for spectral conversion, J. Phys. D: Appl. Phys. **48**, 435103 (2015).

[65] S. K. Lee, H. Chang, C.-H. Han, H.-J. Kim, H. G. Jang, and H. D. Park, Electronic structures and luminescence properties of $YNbO_4$ and $YNbO_4$:Bi, J. Solid State Chem. **156**, 267 (2001).

[66] P. Deák, Q. Duy Ho, F. Seemann, B. Aradi, M. Lorke, and T. Frauenheim, Choosing the correct hybrid for defect calculations: A case study on intrinsic carrier trapping in $\beta - Ga_2O_3$, Phys. Rev. B **95**, 075208 (2017).

[67] A. Seidl, A. Görling, P. Vogl, J. A. Majewski, and M. Levy, Generalized Kohn-Sham schemes and the band-gap problem, Phys. Rev. B **53**, 3764 (1996).

[68] J. P. Perdew, W. Yang, K. Burke, Z. Yang, E. K. U. Gross, M. Scheffler, G. E. Scuseria, T. M. Henderson, I. Y. Zhang, A. Ruzsinszky, H. Peng, J. Sun, E. Trushin, and A. Görling, Understanding band gaps of solids in generalized Kohn-Sham theory, Proc. Natl. Acad. Sci. USA **114**, 2801 (2017).

[69] E. Y. Lee and Y. J. Kim, Synthesis and luminescence of $YNbO_4$:Eu^{3+}, Tb^{3+} by a flux method, Thin Solid Films **518**, e72 (2010).

[70] W. Schipper, M. Hoogendorp, and G. Blasse, The luminescence and X-ray storage properties of Pr^{3+} and Ce^{3+} in $YNbO_4$ and M'-$YTaO_4$, J. Alloys Compd. **202**, 283 (1993).

[71] J. C. Phillips, Generalized Koopmans' Theorem, Phys. Rev. **123**, 420 (1961).

[72] P. Boutinaud, E. Pinel, M. Oubaha, R. Mahiou, E. Cavalli, and M. Bettinelli, Making red emitting phosphors with Pr^{3+}, Opt. Mater. **28**, 9 (2006).

[73] Y. Zhou, Q. Ma, M. Lü, Z. Qiu, and A. Zhang, Combustion synthesis and photoluminescence properties of $YNbO_4$-based nanophosphors, J. Phys. Chem. C **112**, 19901 (2008).

[74] P. Boutinaud, P. Putaj, R. Mahiou, E. Cavalli, A. Speghini, and M. Bettinelli, Quenching of lanthanide emission by intervalence charge transfer in crystals containing closed shell transition metal ions, Spectrosc. Lett. **40**, 209 (2007).

[75] V. Wang, N. Xu, J.-C. Liu, G. Tang, and W.-T. Geng, VASPKIT: A user-friendly interface facilitating high-throughput computing and analysis using VASP code, Comput. Phys. Commun. **267**, 108033 (2021).

[76] K. Momma and F. Izumi, *VESTA3* for three-dimensional visualization of crystal, volumetric and morphology data, J. Appl. Crystallogr. **44**, 1272 (2011).